

THE AGES, METALLICITIES, AND ELEMENT ABUNDANCE RATIOS OF MASSIVE QUENCHED GALAXIES AT $z \simeq 1.6$ *

M. ONODERA¹, C. M. CAROLLO¹, A. RENZINI², M. CAPPPELLARI³, C. MANCINI^{2,4}, N. ARIMOTO^{5,6,7},
E. DADDI⁸, R. GOBAT^{8,9}, V. STRAZZULLO^{8,10}, S. TACCHELLA¹, AND Y. YAMADA⁷

¹Institute for Astronomy, ETH Zürich, Wolfgang-Pauli-strasse 27, 8093 Zürich, Switzerland; monodera@phys.ethz.ch

²INAF-Osservatorio Astronomico di Padova, Vicolo dell'Osservatorio 5, I-35122, Padova, Italy

³Sub-department of Astrophysics, Department of Physics, University of Oxford, Denys Wilkinson Building, Keble Road, Oxford OX1 3RH, UK

⁴Dipartimento di Fisica e Astronomia di Padova, Università di Padova, Vicolo dell'Osservatorio, 3, I-35122, Padova, Italy

⁵Graduate University for Advanced Studies, 2-21-1 Osawa, Mitaka, Tokyo, Japan

⁶Subaru Telescope, 650 North A'ohoku Place, Hilo, HI 96720, USA

⁷National Astronomical Observatory of Japan, 2-21-1 Osawa, Mitaka, Tokyo, Japan

⁸CEA, Laboratoire AIM-CNRS-Université Paris Diderot, Irfu/SAP, Orme des Merisiers, F-91191 Gif-sur-Yvette, France

⁹School of Physics, Korea Institute for Advanced Study, Heogiro 85, Seoul 130-722, Korea

¹⁰Department of Physics, Ludwig-Maximilians-Universität, Scheinerstr. 1, D-81679 München, Germany

Received 2014 November 13; accepted 2015 May 26; published 2015 July 30

ABSTRACT

We investigate the stellar population properties of a sample of 24 massive quenched galaxies at $1.25 < z_{\text{spec}} < 2.09$ identified in the COSMOS field with our Subaru/Multi-object Infrared Camera and Spectrograph near-IR spectroscopic observations. Tracing the stellar population properties as close to their major formation epoch as possible, we try to put constraints on the star formation history, post-quenching evolution, and possible progenitor star-forming populations for such massive quenched galaxies. By using a set of Lick absorption line indices on a rest-frame optical composite spectrum, the average age, metallicity $[Z/H]$, and α -to-iron element abundance ratio $[\alpha/\text{Fe}]$ are derived as $\log(\text{age}/\text{Gyr}) = 0.04^{+0.10}_{-0.08}$, $[Z/H] = 0.24^{+0.20}_{-0.14}$, and $[\alpha/\text{Fe}] = 0.31^{+0.12}_{-0.12}$, respectively. If our sample of quenched galaxies at $\langle z \rangle = 1.6$ is evolved passively to $z = 0$, their stellar population properties will align in excellent agreement with local counterparts at similar stellar velocity dispersions, which qualifies them as progenitors of local massive early-type galaxies. Redshift evolution of stellar population ages in quenched galaxies combined with low redshift measurements from the literature suggests a formation redshift of $z_f \sim 2.3$, around which the bulk of stars in these galaxies have been formed. The measured $[\alpha/\text{Fe}]$ value indicates a star formation timescale of $\lesssim 1$ Gyr, which can be translated into a specific star formation rate of $\simeq 1 \text{ Gyr}^{-1}$ prior to quenching. Based on these findings, we discuss identifying possible progenitor star-forming galaxies at $z \simeq 2.3$. We identify normal star-forming galaxies, i.e., those on the star-forming main sequence, followed by a rapid quenching event, as likely precursors of the quenched galaxies at $\langle z \rangle = 1.6$ presented here.

Key words: galaxies: abundances – galaxies: evolution – galaxies: formation – galaxies: high-redshift – galaxies: stellar content

1. INTRODUCTION

Galaxies at any cosmic epoch appear to spend most of their active phases on the so-called “main sequence” of star-forming galaxies in which the star formation rate (SFR) is tightly correlated with the galaxy stellar mass (M), with a scatter of only ~ 0.3 dex (e.g., Brinchmann et al. 2004; Daddi et al. 2007; Elbaz et al. 2007; Noeske et al. 2007; Pannella et al. 2009, 2015; Magdis et al. 2010; Peng et al. 2010b; Karim et al. 2011; Rodighiero et al. 2011, 2014; Salmi et al. 2012; Whitaker et al. 2012b, 2014; Kashino et al. 2013; Speagle et al. 2014). In several of these studies the star-forming main sequence has a slope that is nearly independent of redshift, while in others it evolves appreciably. However, all studies agree that the normalization evolves strongly, and compared to the present-day universe, is a factor of ~ 20 higher in SFRs with a given stellar mass near $z \sim 2$, with a nearly constant scatter of ~ 0.3 dex. This suggests that star formation in galaxies on the main sequence is self-regulated in a quasi-steady state, fed by the accretion of cold gas coming in and

powering galactic winds going out (Dekel et al. 2009; Bouché et al. 2010; Davé et al. 2012; Lilly et al. 2013; see Kelson 2014 for a different interpretation of the star-forming main sequence).

Passively evolving galaxies that show fully quenched or barely detectable amounts of star-forming activity have also been identified out to $z \sim 2$ and beyond (e.g., Cimatti et al. 2004, 2008; Glazebrook et al. 2004; Daddi et al. 2005; Kriek et al. 2008; Onodera et al. 2010, 2012; van de Sande et al. 2011, 2013; Toft et al. 2012; Bedregal et al. 2013; Bezanson et al. 2013; Gobat et al. 2013; Whitaker et al. 2013; Belli et al. 2014a, 2014b; Krogager et al. 2014), including one at $z = 3$ (Gobat et al. 2012). Various physical processes responsible for quenching star formation in star-forming main-sequence galaxies are currently considered and debated, such as the suppression of cold gas streams in dark matter halos above a critical mass (Birboim & Dekel 2003), radio-mode (Croton et al. 2006), or quasar-mode (Hopkins et al. 2006) feedback from active galactic nuclei (AGNs), and the suppression of disk instabilities against fragmentation into massive star-forming clumps (so-called “morphological” or “gravitational” quenching, Martig et al. 2009; Genzel et al. 2014b).

* Based on data collected at the Subaru telescope, which is operated by the National Astronomical Observatory of Japan. (Proposal IDs: S09A-043, S10A-058, and S11A-075.)

Fossil records imprinted in the stellar populations of quenched galaxies (i.e., age, metallicity $[Z/H]$, and α -element-to-iron abundance ratio $[\alpha/Fe]$) give clues as to when quenching took place, and the timescales over which the stellar mass built up. Extensive studies have been carried out to measure these quantities in local quenched galaxies, especially using a set of absorption line strength indicators known as the Lick indices (e.g., Burstein et al. 1984; Carollo et al. 1993; Worthey et al. 1994; Worthey & Ottaviani 1997; Trager et al. 1998, 2000, 2008; Thomas et al. 2005, 2010; Sánchez-Blázquez et al. 2006a; Yamada et al. 2006; Kuntschner et al. 2010; Spolaor et al. 2010; Greene et al. 2012, 2013). These studies indicate that in the local universe the most massive ($M > 10^{11} M_{\odot}$) among the quenched galaxies are the oldest, most metal-rich, and most α -element enhanced, i.e., they typically host $\simeq 10$ Gyr old stellar populations, with solar or above solar metallicities and enhanced $[\alpha/Fe]$ ratios up to about 0.5 dex compared to the solar ratio. The enhanced $[\alpha/Fe]$ ratio favors a dominance of Type II supernovae (SNe II) in chemical enrichment relative to SNe Ia, which in turn implies a short timescale for star formation and quenching (e.g., Matteucci & Greggio 1986; Thomas et al. 1999).

Stellar population ages of the quenched galaxy population have been used as an indicator of the formation epoch when the bulk of stars were formed (e.g., Kelson et al. 2001). These ages are derived via the strengths of Balmer absorption lines such as $H\beta$, $H\gamma$, and $H\delta$ that change rapidly in stellar populations younger than several Gyr, while the changes are much milder for older ages. For instance, stellar population synthesis models by Thomas et al. (2011b) predict that for solar metallicity and element abundance ratios, the Lick $H\beta$ index changes by $\sim 2 \text{ \AA}$ for ages between 1 and 5 Gyr, while the change becomes only $\simeq 0.3 \text{ \AA}$ between 5 and 10 Gyr. The reduced age sensitivity of the $H\beta$ index at older ages can then make it difficult to estimate the formation redshift of local quenched galaxies, even if very high signal-to-noise ratios (S/N), e.g., $\gg 100$, can be achieved for such nearby objects (e.g., Yamada et al. 2006; Conroy et al. 2014). At higher redshifts, where the galaxies are closer to their quenching epoch, the Lick Balmer-line indices are more sensitive to age. Therefore the formation redshift of quenched galaxies and of their precursors can be more precisely estimated.

Stellar population analyses based on the Lick spectral indices have so far reached intermediate redshifts ($z \sim 0.9$), indicating high metallicities, $[\alpha/Fe]$ ratios for the most massive quenched systems, similar to those of local quenched galaxies of the same mass, and a formation redshift of $z_f > 2$ (Kelson et al. 2006; Jørgensen & Chiboucas 2013, see also Choi et al. 2014; Gallazzi et al. 2014 for the results based on different approaches).

In this paper we construct a composite spectrum by stacking the spectra of 24 quenched galaxies at $1.25 < z < 2.09$ taken with Multi-object Infrared Camera and Spectrograph (MOIRCS; Ichikawa et al. 2006; Suzuki et al. 2008) on the Subaru telescope, thus pushing the measurement of stellar population parameters via Lick indices out to an average redshift of $\langle z \rangle = 1.6$. Using the measured properties in galaxies still close to their quenching epoch we derive more precise estimates for their formation timescale and time elapsed since their quenching, and identify their possible star-forming precursors.

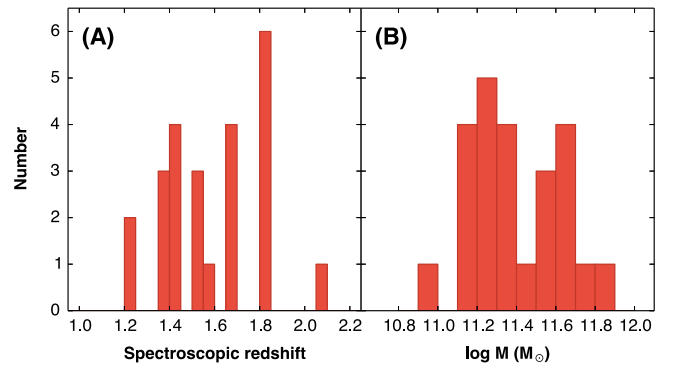


Figure 1. Histograms of (A) the spectroscopic redshifts and (B) the stellar masses of the 24 galaxies in the sample.

The paper is organized as follows. In Section 2, we present the sample galaxies and their composite spectrum. The measurement of Lick indices and the derivation of stellar population parameters (age, $[Z/H]$, and $[\alpha/Fe]$) are described in Sections 3 and 4, respectively. In Section 5 we first discuss a possible selection bias in our spectroscopic sample, and then discuss the star formation history (SFH) of the quenched galaxies at $\langle z \rangle = 1.6$, along with their possible descendants and precursors at different redshifts. Finally, we summarize our results in Section 6. Throughout the analysis, we adopt a Λ -dominated cold dark matter cosmology with cosmological parameters of $H_0 = 70 \text{ km s}^{-1} \text{ Mpc}^{-1}$, $\Omega_m = 0.3$, and $\Omega_\Lambda = 0.7$ and AB magnitude system (Oke & Gunn 1983).

2. DATA

2.1. Sample

We selected 24 quenched galaxies with robust spectroscopic redshifts in the range $1.25 < z < 2.09$, derived from spectra obtained with the MOIRCS instrument at the Subaru telescope. For a detailed description of the observations and data reduction, refer to Onodera et al. (2012). Briefly, all objects were first selected as passive BzK galaxies (Daddi et al. 2004) based on the near-IR-selected photometric catalog in the COSMOS field (Scoville et al. 2007; McCracken et al. 2010), with two additional criteria: a photometric redshift $z \gtrsim 1.4$ and no mid-IR detection at $24 \mu\text{m}$ with MIPS at the *Spitzer Space Telescope*. The redshift selection allowed us to observe the 4000 \AA break in most cases with the adopted instrument setup. The objects were integrated for 7–9 hr each, under 0.4–1.2 arcsec seeing conditions, with 0.7 arcsec slit width, and using the zJ500 grism, which gives a spectral resolution of $R \sim 500$. The data were reduced with the standard MCSMDP package (Yoshikawa et al. 2010), including flat-fielding, bad pixel and cosmic-ray removal, sky subtraction, distortion correction, and wavelength calibration by OH sky lines. Flux calibration was performed with A0V stars taken in the same nights as the object spectra and the slit-loss was corrected by scaling the continuum flux to the J - or H -band broadband fluxes. We measured the redshifts by cross-correlating the spectra either with simple stellar population (SSP) template spectra (Bruzual & Charlot 2003) or with stellar template spectra (Sánchez-Blázquez et al. 2006b).

Figure 1(A) shows the redshift distribution of the sample. The mean and median redshifts are 1.56 and 1.59, respectively, with a standard deviation of 0.21. Virtually all objects belong to redshift spikes. Among the 24 objects, 14 have already been

published (Onodera et al. 2010, 2012) and the other 10 objects were identified during an observing run in 2011. We have removed 4 objects among the 18 identified in Onodera et al. (2012): object ID 313880 was removed because of the presence of *Spitzer*/MIPS 24 μm emission, which may originate from star-forming activity or an AGN, and objects ID 209501, 253431, and 275414 were removed due to the lower confidence class for their spectroscopic redshifts.

2.2. Stellar Masses and Specific SFRs

We estimated stellar masses and SFRs by fitting synthetic spectral energy distributions to fluxes through broadbands extending from the *u* to the *Spitzer*/IRAC 8.5 μm band and using the FAST code¹¹ (Kriek et al. 2009) as described in detail in Onodera et al. (2012). In brief, we find a best-fit model within a grid of templates based on the 2007 version of Bruzual & Charlot’s (2003) population synthesis models¹² adopting an exponentially declining SFH with various *e*-folding times τ . We allow for dust extinction adopting the extinction law by Calzetti et al. (2000). The Salpeter initial mass function (IMF; Salpeter 1955) was adopted, which may be appropriate for galaxies as massive as those in our sample (Shetty & Cappellari 2014). Age, mass, τ and metallicity are then the results of the procedure, having fixed the redshifts at the spectroscopic values. The resulting stellar masses¹³ are in the range $11 < \log M/M_{\odot} < 11.9$, with a median of $\log M/M_{\odot} = 11.4$ as shown in Figure 1(B).

The MOIRCS spectra confirm the quenched nature of these galaxies, as they show no emission lines, a strong break at rest-frame 4000 Å, and strong absorption lines typical of old stellar populations. All objects have specific SFRs (sSFR \equiv SFR/*M*) below 10^{-11} yr^{-1} , as derived from the best-fit exponentially declining SFH, which corresponds to a specific star formation rate (sSFR) of about two orders of magnitude lower than that of main-sequence galaxies at a similar redshift (e.g., Kashino et al. 2013).

2.3. Structural Parameters

The effective radii, r_e , and Sérsic indices, n , of the 10 additional objects from the 2011 observing run were measured in exactly the same way as the rest of the sample presented in Onodera et al. (2012). In brief, we used GALFIT¹⁴ version 3.0 (Peng et al. 2002, 2010a) to carry out a 2D Sérsic profile fitting for the images taken in the F814W filter with the Advanced Camera for Surveys on the *Hubble Space Telescope* (*HST*; Koekemoer et al. 2007; Massey et al. 2010). For each galaxy, we constructed the point-spread function (PSF) from nearby unsaturated stars. We estimated the sky background using three different methods: (1) the sky as a free parameter; (2) the sky fixed to the so-called pedestal GALFIT estimate; and (3) the sky manually measured from empty regions near the sample galaxy. We used the midpoints between the minimum and maximum of these runs, and half of the ranges as associated errors, for effective radius, Sérsic parameter, total magnitude, and axial ratio. GALFIT did not converge for objects 406178 and 531916 due to low surface brightness in the F814W filter.

Object IDs, coordinates, spectroscopic redshift, stellar mass, effective radius, and Sérsic index for all of the galaxies in the sample are listed in Table 1.

2.4. Composite Spectrum

In order to achieve the high S/N needed for the measurement of the Lick indices, we constructed a composite spectrum by stacking the individual galaxy spectra in the same way as described in Onodera et al. (2012): all spectra were registered to the rest-frame wavelength by linearly interpolating on a 1 Å interval, and normalized by the mean flux at $4500 < \lambda(\text{Å}) < 5200$ in the rest-frame. Noise spectra were also registered to the same rest-frame wavelength scale, but interpolated in quadrature. Then the spectra were co-added with weights proportional to the inverse square of the S/N at each wavelength pixel.

To correct for possible sampling bias, we computed the associated noise spectrum with the *jackknife* method as

$$\sigma_{\text{Jack}}^2 = \frac{N-1}{N} \sum_{i=1}^N (f - f_{(i)})^2, \quad (1)$$

where N ($=24$) is the number of objects in the sample, f is the flux of the stacked spectrum of all N spectra, and $f_{(i)}$ is the flux of a stacked spectrum made of $N-1$ spectra by removing the i th spectrum. We then corrected the stacked spectrum for the bias using

$$f' = f - (N-1) (\langle f_{(i)} \rangle - f) \quad (2)$$

where $\langle f_{(i)} \rangle = \frac{1}{N} \sum_{i=1}^N f_{(i)}$. The typical correction factor is very small ($<1\%$) in the wavelength range studied in this work, but it is a more realistic estimate of noise due to OH sky line residuals which vary significantly from pixel to pixel. We have adopted f' and σ_{Jack} as the final stacked spectrum and 1σ noise spectrum, respectively.

The resulting composite spectrum, corresponding to an equivalent integration time of about 200 hr on Subaru/MOIRCS, is shown in Figure 2. This figure shows several clear absorption features, including the 4000 Å break, Ca II H +K lines, various Balmer absorption lines, the *G*-band, and Mg and Fe absorption features, which will be used in the next section to derive the stellar population parameters.

3. MEASUREMENT OF LICK ABSORPTION LINE INDICES

We measured the Lick indices on the stacked spectrum using LECTOR,¹⁵ following the definition given by Worthey & Ottaviani (1997) and Trager et al. (1998). We used the *jackknife* method to measure each index following Equations (1) and (2): we measured the indices on each $f_{(i)}$ and derived the bias-corrected index values and corresponding 1σ error bars. The Lick indices measured on the stacked spectrum with the observed spectral resolution are listed in the second column in Table 2.

¹¹ <http://astro.berkeley.edu/~mariska/FAST.html>

¹² <http://www.bruzual.org/cb07/>

¹³ Sum of living stars and remnants.

¹⁴ <http://users.obs.carnegiescience.edu/peng/work/galfit/galfit.html>

¹⁵ http://www.iac.es/galeria/vazdekis/vazdekis_software.html

Table 1
Properties of the Sample Galaxies

| ID | R.A. (deg) | Decl. (deg) | z_{spec} | $\log M/M_{\odot}$ | r_e (kpc) | Sérsic n |
|--------|---------------|----------------|---------------------|-------------------------|-----------------|---------------|
| 254025 | 150.6187115 | 2.0371363 | 1.8228 ± 0.0006 | $11.64^{+0.15}_{-0.03}$ | 3.16 ± 0.61 | 3.4 ± 0.4 |
| 217431 | 150.6646939 | 1.9497545 | 1.4277 ± 0.0015 | $11.82^{+0.03}_{-0.15}$ | 7.19 ± 1.95 | 3.8 ± 0.6 |
| 307881 | 150.6484873 | 2.1539903 | 1.4290 ± 0.0009 | $11.75^{+0.03}_{-0.11}$ | 2.68 ± 0.12 | 2.3 ± 0.1 |
| 233838 | 150.6251048 | 1.9889180 | 1.8199 ± 0.0016 | $11.64^{+0.16}_{-0.25}$ | 2.25 ± 0.31 | 3.1 ± 0.3 |
| 277491 | 150.5833512 | 2.0890266 | 1.8163 ± 0.0038 | $11.56^{+0.11}_{-0.12}$ | 2.46 ± 0.11 | 1.0^a |
| 250093 | 150.6053729 | 2.0288998 | 1.8270 ± 0.0010 | $11.25^{+0.13}_{-0.08}$ | 3.00 ± 0.15 | 1.0^a |
| 263508 | 150.5677283 | 2.0594318 | 1.5212 ± 0.0009 | $11.11^{+0.10}_{-0.21}$ | 0.86 ± 0.03 | 3.2 ± 0.2 |
| 269286 | 150.5718552 | 2.0712204 | 1.6593 ± 0.0006 | $11.26^{+0.02}_{-0.28}$ | 1.03 ± 0.12 | 5.0 ± 0.7 |
| 240892 | 150.6432950 | 2.0073169 | 1.5494 ± 0.0009 | $11.20^{+0.19}_{-0.13}$ | 1.29 ± 0.13 | 3.0 ± 0.3 |
| 205612 | 150.6542714 | 1.9233323 | 1.6751 ± 0.0045 | $11.15^{+0.13}_{-0.06}$ | 2.08 ± 0.28 | 2.4 ± 0.3 |
| 251833 | 150.6293675 | 2.0336620 | 1.4258 ± 0.0006 | $10.99^{+0.27}_{-0.05}$ | 1.61 ± 0.09 | 2.1 ± 0.1 |
| 228121 | 150.5936156 | 1.9754018 | 1.8084 ± 0.0015 | $11.39^{+0.14}_{-0.03}$ | 2.78 ± 0.86 | 4.1 ± 0.9 |
| 321998 | 150.7093826 | 2.1863891 | 1.5226 ± 0.0009 | $11.28^{+0.12}_{-0.09}$ | 1.83 ± 0.34 | 4.4 ± 0.6 |
| 299038 | 150.7091894 | 2.1369001 | 1.8196 ± 0.0010 | $11.30^{+0.08}_{-0.15}$ | 0.96 ± 0.02 | 1.9 ± 0.0 |
| 519818 | 150.0124421 | 2.6406856 | 2.0879 ± 0.0010 | $11.37^{+0.28}_{-0.24}$ | 1.69 ± 0.36 | 5.4 ± 0.7 |
| 526785 | 150.0057599 | 2.6548908 | 1.2454 ± 0.0383 | $11.44^{+0.04}_{-0.30}$ | 4.95 ± 0.54 | 3.1 ± 0.1 |
| 528213 | 150.0199418 | 2.6592730 | 1.3950 ± 0.0004 | $11.33^{+0.32}_{-0.22}$ | 3.06 ± 0.27 | 3.2 ± 0.2 |
| 535544 | 150.0027420 | 2.6748955 | 1.2452 ± 0.0003 | $11.68^{+0.05}_{-0.30}$ | 5.73 ± 1.22 | 4.2 ± 0.5 |
| 531916 | 149.9828887 | 2.6689945 | 1.3569 ± 0.0333 | $11.14^{+0.28}_{-0.41}$ | ... | ... |
| 533754 | 150.0190505 | 2.6731339 | 1.3956 ± 0.0003 | $11.60^{+0.04}_{-0.18}$ | 2.42 ± 0.08 | 1.3 ± 0.1 |
| 543256 | 150.0179738 | 2.6948240 | 1.4340 ± 0.0008 | $11.29^{+0.19}_{-0.22}$ | 3.34 ± 0.39 | 3.7 ± 0.3 |
| 401700 | 150.2914647 | 2.3715033 | 1.6501 ± 0.0003 | $11.16^{+0.25}_{-0.14}$ | 1.73 ± 0.40 | 4.5 ± 1.0 |
| 411647 | 150.2915999 | 2.3956325 | 1.6525 ± 0.0008 | $11.56^{+0.08}_{-0.31}$ | 2.67 ± 0.41 | 1.8 ± 0.3 |
| 406178 | 150.2881135 | 2.3813900 | 1.5718 ± 0.0037 | $11.56^{+0.16}_{-0.60}$ | ... | ... |

Notes. Effective radii are circularized, i.e., $r_e = a\sqrt{q}$, where a and q are semimajor axis length and axis ratio, respectively.

^a The GALFIT run was carried out by fixing $n = 1$ (see Onodera et al. 2012).

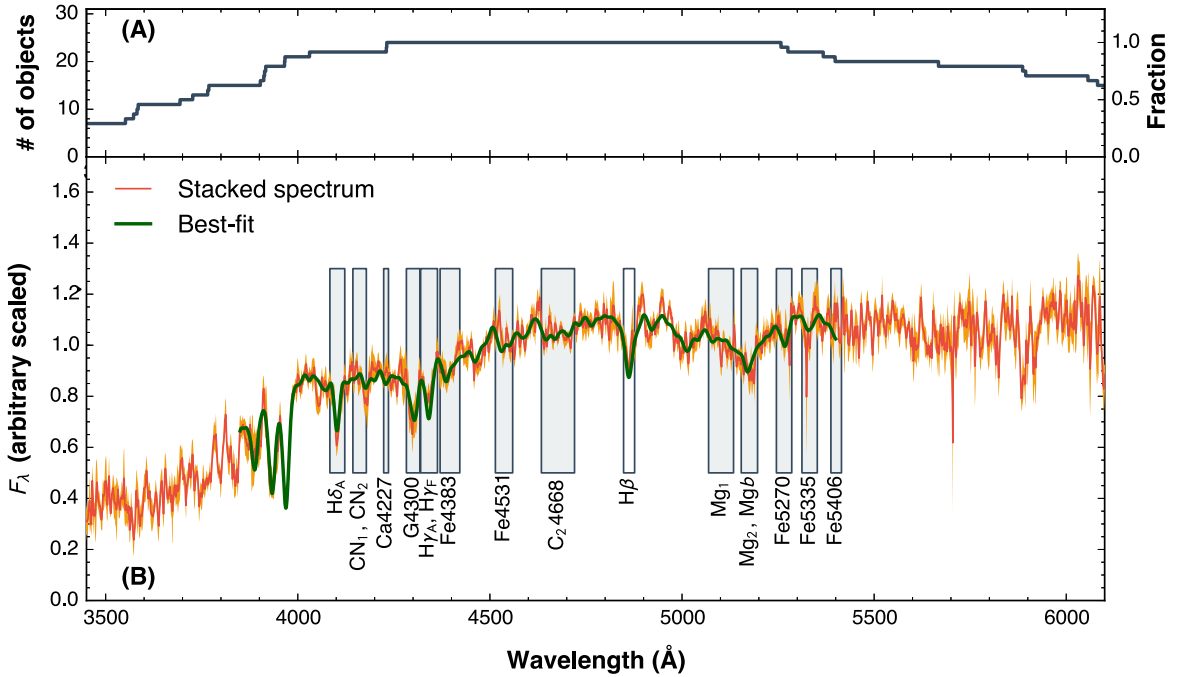


Figure 2. Composite rest-frame optical spectrum of the 24 quenched galaxies at $z \sim 1.6$. (A): the number (left axis) and fraction (right axis) of spectra that have been stacked at each wavelength. (B): the stacked spectrum and associated 1σ error (orange solid line and filled region, respectively). The green solid line shows the best-fit combination of stellar spectra (Sánchez-Blázquez et al. 2006b), using pPXF (Cappellari & Emsellem 2004). The rectangles show the wavelength ranges used to measure the Lick indices of the stacked spectrum, though the $H\beta$ index is not used in our stellar population analysis.

Table 2
Lick Indices Measured in the Stacked Spectrum

| Index | Raw Measurement | Broadening Corrected |
|---------------------|------------------|----------------------|
| H δ_A | 4.27 \pm 0.69 | 4.26 \pm 0.72 |
| H δ_F | 3.26 \pm 0.74 | 3.61 \pm 0.79 |
| CN ₁ | -0.08 \pm 0.02 | -0.08 \pm 0.02 |
| CN ₂ | -0.03 \pm 0.03 | -0.02 \pm 0.03 |
| Ca4227 | -0.15 \pm 0.48 | -0.23 \pm 0.75 |
| G4300 | 4.45 \pm 1.31 | 4.90 \pm 1.34 |
| H γ_A | -0.88 \pm 1.34 | -0.95 \pm 1.38 |
| H γ_F | 1.14 \pm 0.73 | 1.38 \pm 0.80 |
| Fe4383 | 2.67 \pm 1.38 | 3.57 \pm 1.59 |
| Fe4531 | 0.51 \pm 1.12 | 0.70 \pm 1.38 |
| C ₂ 4668 | 4.71 \pm 1.09 | 5.51 \pm 1.25 |
| H β | 2.36 \pm 0.60 | 2.68 \pm 0.73 |
| Mg ₁ | 0.09 \pm 0.02 | 0.10 \pm 0.02 |
| Mg ₂ | 0.18 \pm 0.01 | 0.18 \pm 0.01 |
| Mgb | 2.13 \pm 0.72 | 2.88 \pm 0.97 |
| Fe5270 | 1.53 \pm 0.89 | 2.09 \pm 1.18 |
| Fe5335 | 1.69 \pm 0.71 | 3.25 \pm 1.38 |
| Fe5406 | 0.96 \pm 1.05 | 1.88 \pm 2.03 |

Note. CN₁, CN₂, Mg₁, and Mg₂ indices are in a unit of magnitude; otherwise, indices are in a unit of Å. H δ_F and H β indices are not used in the analysis presented in this work.

3.1. Broadening Measurement and Stellar Velocity Dispersion

Measurements of Lick indices strongly depend on the broadening of the spectra: the larger the broadening, the shallower the absorption features and the more likely that part of the spectral feature falls outside the index windows. The total broadening (σ_{tot}) is a combination of the intrinsic stellar velocity dispersion (σ_*) of the object, instrumental resolution (σ_{instr}), and stacking procedure reflecting redshift errors (σ_{stack}), and can be expressed as $\sigma_{\text{tot}}^2 = \sigma_*^2 + \sigma_{\text{instr}}^2 + \sigma_{\text{stack}}^2$ (Cappellari et al. 2009). We measured $\sigma_{\text{tot}} = 457 \pm 23 \text{ km s}^{-1}$ by using the penalized pixel-fitting method (pPXF¹⁶; Cappellari & Emsellem 2004) with template stellar spectra from the MILES database¹⁷ (Sánchez-Blázquez et al. 2006b). During the pPXF run, we masked wavelength ranges that are potentially contaminated by emission lines, namely H γ , H β , and [O III] $\lambda\lambda 4959, 5007$. The best-fit combination of the templates is shown with the green solid line in Figure 2.

Adopting the same procedure as Cappellari et al. (2009), σ_{stack} can be computed using $\sigma_{\text{stack}} \approx c\Delta z/(1+z)$, where c is the speed of light and Δz is the redshift error. We computed σ_{stack} for all objects used for stacking, and derived the average as $\sigma_{\text{stack}} = 101 \pm 83 \text{ km s}^{-1}$ by using the bi-weight estimator (Beers et al. 1990). This σ_{stack} may be a conservative estimate, because objects with larger redshift errors have lower S/Ns and thus have less weight in the stacked spectrum. Adopting the instrumental resolution of $\sigma_{\text{instr}} = 300 \pm 7 \text{ km s}^{-1}$ (Onodera et al. 2010), by combining these numbers together, the stellar velocity dispersion of the stacked spectrum is estimated to be $\sigma_* = 330 \pm 41 \text{ km s}^{-1}$. This is in good agreement with the average stellar velocity dispersion, $\langle\sigma_{\text{inf}}\rangle = 298 \pm 71 \text{ km s}^{-1}$, inferred from the structural parameters and stellar masses of the objects (Bezanson et al. 2011).

3.2. Broadening Correction

The resulting σ_{tot} is in general larger than that of the original Lick/IDS system which is $\simeq 200\text{--}360 \text{ km s}^{-1}$ depending on the indices. Therefore, the indices measured on our stacked spectrum have to be corrected to the Lick resolution. For this purpose, we computed the Lick indices on the MILES SSP models (Vazdekis et al. 2010) by convolving the model spectra with the original Lick resolution (Worthey & Ottaviani 1997; Schiavon 2007) and our resolution of $\sigma_{\text{tot}} = 460 \text{ km s}^{-1}$. The MILES SSP models¹⁸ were constructed with a unimodal IMF with a slope of 1.3 (equivalent to the Salpeter IMF), $-2.32 < [M/H] < 0.22$ and age from 0.06 Gyr to that of the universe at the corresponding redshift. We restricted the models to be in the safe range of parameters by setting `Mode=SAFE`. Comparing the indices measured with various broadenings, we found tight linear relations ($\lesssim 1\%$ scatter) for all the indices and we used these relations to convert our values to those with the Lick/IDS resolution. The Lick indices corrected for the spectral resolution are listed in the third column in Table 2.

4. STELLAR POPULATION PARAMETERS FROM LICK INDICES

In the following analysis we use a series of Lick indices for which synthetic models accurately reproduce those of Galactic globular clusters, as shown by Thomas et al. (2011b), namely: H δ_A , H γ_A , H γ_F , CN₁, CN₂, Ca4227, G4300, C₂4668, Mg₁, Mg₂, Mgb, Fe4383, Fe4531, Fe5270, Fe5335, and Fe5406. The H β index is widely used as an age indicator since it is less contaminated by metal lines, but it was not used in this analysis for the following two reasons. First, there may be a contribution from emission partially filling the absorption. Comparing the stacked spectra and best-fit template returned by pPXF, we measured a 3σ upper limit of $\simeq 1 \text{ Å}$ to the equivalent width of the H β emission line. On the other hand, the higher-order Balmer lines such as H γ and H δ are less affected by emission, with an equivalent width $\lesssim 0.5 \text{ Å}$. Second, the H β indices in Galactic globular clusters are too weak for even the oldest SSP models to reproduce (Poole et al. 2010). We would like to note, however, that the inclusion of H β to the set of indices above does not affect the results and conclusions presented here.

We derived the stellar population parameters, age, $[Z/H]$, and $[\alpha/Fe]$, by comparing the Lick indices measured on the composite spectrum with those calculated from SSP models with variable abundance ratios¹⁹ (Thomas et al. 2011b). Since the models give absolute fluxes by making use of flux-calibrated stellar spectral templates, the observed indices do not need to be converted to the Lick/IDS response. The models span the parameter space $0.1 < \text{age/Gyr} < 15$, $-2.25 < [Z/H] < 0.67$, and $-0.3 < [\alpha/Fe] < 0.5$ and adopt the Salpeter IMF.

For each index, we constructed a three-dimensional model grid of $\log(\text{age})$, $[Z/H]$, and $[\alpha/Fe]$ with a uniform interval of 0.025 dex for all three parameters and on this grid we computed the $\chi^2 = \sum_{\text{index}} (I_{\text{index}}^{\text{obs}} - I_{\text{index}}^{\text{model}})^2 / \sigma_{\text{index}}^2$, where $I_{\text{index}}^{\text{obs}}$ and $I_{\text{index}}^{\text{model}}$ are observed and model indices, respectively, and σ_{index} is the 1σ error of the observed indices. Then we converted the χ^2 to a probability distribution $p \propto \exp(-\chi^2/2)$, and normalized it such that $\int p d \log(\text{age}) d[Z/H] d[\alpha/Fe] = 1$.

¹⁶ <http://purl.org/cappellari/software>

¹⁷ <http://miles.iac.es/>

¹⁸ <http://miles.iac.es/pages/webtools/tune-ssp-models.php>

¹⁹ <http://www.icg.port.ac.uk/~thomasd/tmj.html>

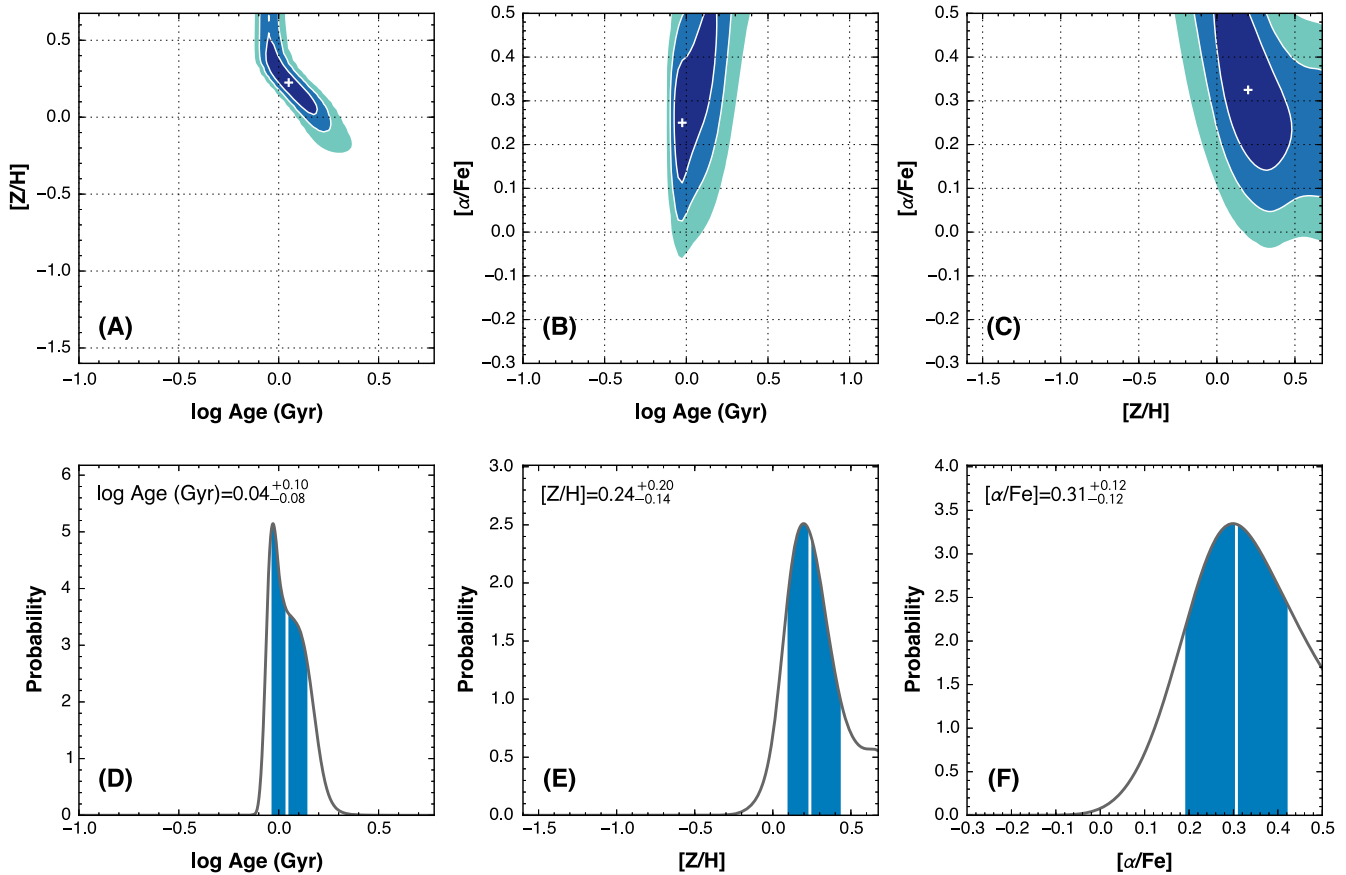


Figure 3. Probability distributions of stellar population parameters for the quenched galaxies at $z \sim 1.6$. Top: two-dimensional probability distributions in the (A) age– $[Z/H]$, (B) age– $[\alpha/Fe]$, and (C) $[Z/H]$ – $[\alpha/Fe]$ planes. Cross symbols show the peak of the probability distributions and the contours indicate the areas that enclose 68.2%, 95.4%, and 99.7% of the probability distributions, respectively. Bottom: one-dimensional probability distributions for (D) age, (E) $[Z/H]$, and (F) $[\alpha/Fe]$. The vertical white solid lines indicate the median values, and the left and right edges of the filled regions define the 16 and 84 percentiles, respectively.

The resulting best-fit stellar population parameters are shown as white plus signs in Figure 3, which corresponds to the minimum reduced- χ^2 of ~ 2.0 . The reduced- χ^2 drops to 1.37 by removing the CN indices from the fit, while the best-fit parameters do not change at all. This poor fit due to the CN indices is not surprising, as nitrogen is not a free parameter in the fit (see also Thomas et al. 2011a, 2011b). Confidence regions enclosing 68.2%, 95.4%, and 99.7% of the total volume of the projected probability distributions are shown in the top panels of Figure 3. The probability distributions are marginalized to a one-dimensional parameter space (bottom panels in Figure 3) by adopting median values for each stellar population parameter and 16 and 84 percentiles as corresponding 1σ confidence intervals, respectively. In this way we have obtained $\log(\text{age}/\text{Gyr}) = 0.04^{+0.10}_{-0.08}$, $[Z/H] = 0.24^{+0.20}_{-0.14}$, and $[\alpha/Fe] = 0.31^{+0.12}_{-0.12}$ for the composite stellar population of our 24 galaxies. Of course, these uncertainties only reflect random errors associated with the measurement of the various indices and the quality of the fits, whereas systematic errors coming from the synthetic models may be significantly larger (e.g., Trager et al. 2008).

5. DISCUSSION

5.1. Bias in the Sample

Spectroscopically identified samples could be biased toward relatively bluer, lower mass-to-light ratio objects, especially at

$z > 1.4$, as pointed out by van de Sande et al. (2014). Although our sample is nearly complete down to $K_{AB} \simeq 21.5$ (Onodera et al. 2012), in this section we investigate potential biases that may affect our sample.

We computed rest-frame $U - V$ and $V - J$ colors of our sample and compared them with the photometric sample of passive BzK-selected galaxies in Figure 4. Since we have extracted the photometric sample for this comparison from a public catalog in the COSMOS field by Muzzin et al. (2013a), we obtained the rest-frame colors using the Muzzin et al. photometry. We ran EAZY²⁰ (Brammer et al. 2008) using the identical template set and input parameters as those used in Muzzin et al., except that redshifts are fixed to the spectroscopic redshifts, and computed the rest-frame colors for U - and V -bands of Maíz Apellániz (2006) and 2MASS J -band. For the photometric sample extracted from the Muzzin et al. catalog, we required the photometry flag of unity, non-detection in *Spitzer*/MIPS 24 μm , and $K_{AB} < 21.5$ to match the selection of our sample, in addition to the standard passive BzK selection criteria (Daddi et al. 2004).

Figure 4 shows that the majority of our sample are classified as “old quenched” according to the Whitaker et al. (2012a) criterion and the overall distribution appears to be consistent with that of the parent sample. Quantitatively, the median colors of our sample and the parent sample are $(V - J, U - V) = (1.16, 1.78)$ and $(V - J, U - V) = (1.10, 1.85)$,

²⁰ <http://www.astro.yale.edu/eazy/>

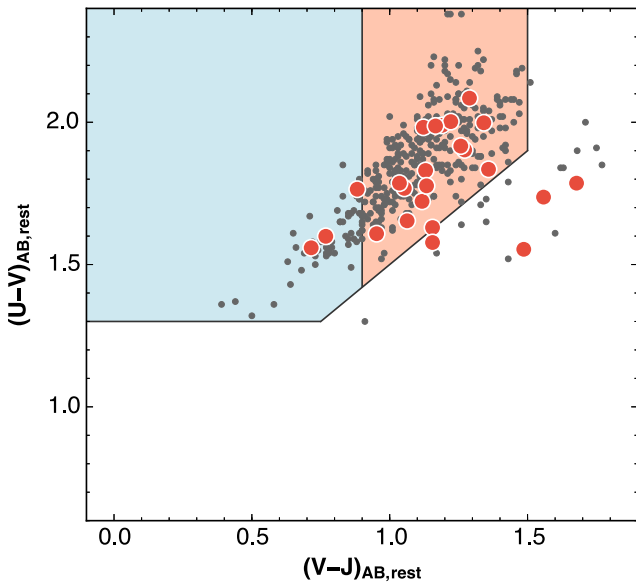


Figure 4. Rest-frame UVJ color-color diagram. Red circles are our quenched galaxies at $\langle z \rangle = 1.6$ with UVJ colors computed as described in Section 5.1. Gray dots represent photometrically selected passive BzK galaxies (Daddi et al. 2004) with reliable photometry, non-detection in *Spitzer*/MIPS 24 μm , and $K_{\text{AB}} < 21.5$ taken from Muzzin et al. (2013a). Blue and red areas indicate regions to separate young and old quiescent galaxies, respectively, while the rest of the diagram classifies galaxies as star-forming (Whitaker et al. 2012a).

respectively. Note that the typical uncertainty in the rest-frame colors is 0.1–0.2 mag (e.g., Williams et al. 2009) and the above differences are consistent within it. One might argue that the UVJ selection cannot perfectly isolate the passive BzK population in the quiescent section of the diagram or vice versa, even though there appears to be no signature of emission lines in our spectroscopic sample. However, we would like to note that both UVJ and BzK diagnostics select quenched galaxies only in a statistical sense and some degree of contamination outside of the quiescent region is not entirely unexpected (see Moresco et al. 2013 for a detailed comparison of various selection methods of passive galaxies at $z < 1$).

Whitaker et al. (2013) have derived stellar population ages of UVJ -selected quiescent galaxies at $1.4 < z < 2.2$ identified in *HST*/WFC3 G141 grism observations from the 3D-*HST* survey (Brammer et al. 2012). The average age is $1.3^{+0.1}_{-0.3}$ Gyr for all quiescent galaxies, which is in excellent agreement with that of our quenched galaxies at similar redshift. They also split the sample into *young* and *old* quiescent galaxies, and the derived ages for both classes are consistent with ours within the uncertainties.

Comparisons of the rest-frame colors with the parent passive BzK sample and of the stellar population ages with the galaxies with similar colors from Whitaker et al. (2013) suggest that our spectroscopic sample is not likely to be biased toward younger ages and appears to be representative of the quenched galaxy population at $\langle z \rangle = 1.6$. However, the comparison discussed here is based on the K -selected sample. Therefore, the lack of apparent bias in our spectroscopic sample with respect to the photometric one does not necessarily mean that there is no bias compared to the entire (e.g., mass-selected) quiescent population.

5.2. Redshift Evolution of Stellar Populations in Quenched Galaxies

Figure 5 compares the stellar population luminosity-weighted age, $[Z/H]$, and $[\alpha/Fe]$ of various sets of quenched galaxies at different redshifts. Having derived an age $\log(\text{age}/\text{Gyr}) = 0.04^{+0.10}_{-0.08}$, or $\simeq 1.1$ Gyr, from the composite spectrum, we calculate that the passive aging over ~ 9.5 Gyr from $\langle z \rangle = 1.6$ to $z = 0$, i.e., to an age of ~ 11 Gyr, will bring the stellar populations of these galaxies to the point indicated by the arrowhead in Figure 5(A). This is in excellent agreement with the luminosity-weighted ages of stellar populations in local quenched galaxies of similar velocity dispersions by Spolaor et al. (2010), who derive the stellar population parameters via Lick indices using stellar population models from Thomas et al. (2003), which are equivalent in this respect to the Thomas et al. (2011b) models adopted in this study.

Figure 5(B) shows the age-redshift relations for different values of the formation redshift z_f (gray solid lines), assuming a single burst of star formation at z_f . In this SSP approximation, the average age of ~ 1.1 Gyr indicates a formation redshift of $2 \lesssim z_f \lesssim 2.5$ for the bulk of the stars. Figure 5(B) also shows the stellar population ages of similarly massive, quenched galaxies in clusters at $z = 0.54, 0.83,$ and 0.89 (Jørgensen & Chiboucas 2013). These are currently the only ages for quenched galaxies at these intermediate epochs with comparable σ that have been derived in a homogeneous way similar to our galaxies, i.e., using the Lick indices and the Thomas et al. (2011b) models to derive the stellar population parameters. Apart from a possible (small) bias due to the special location in high density peaks, these lower redshift cluster galaxies fit remarkably well along the evolutionary trend expected for pure passive evolution from $\langle z \rangle = 1.6$ to $z = 0$.

Furthermore, Figure 5 shows that the derived metallicity $[Z/H] = 0.24^{+0.20}_{-0.14}$, or $\simeq 1.7 Z_{\odot}$, of our composite $\langle z \rangle = 1.6$ galaxies is the same as that of local quenched galaxies of similar velocity dispersion (Spolaor et al. 2010). The two different colors—blue and orange—in the figure correspond to the values measured at the central part of galaxies (within $r_e/8$) and within the effective radius, respectively. The aperture used to extract the spectra of the $\langle z \rangle = 1.6$ sample is about $(2\text{--}3)r_e$. In the case that the galaxy is well resolved, stellar population parameters derived within large radii (e.g., $r > r_e$) converge to those integrated to the effective radius (Kobayashi & Arimoto 1999). However, our sample was observed with an FWHM of the PSF corresponding to $\gtrsim 2r_e$. van de Sande et al. (2013) have examined the aperture correction for velocity dispersion measurements by taking PSF and aperture effects into account for a Sérsic profile and we have followed the same approach to investigate these effects on the derived metallicity. Since radial metallicity gradients in the local quenched galaxies are very steep ($\Delta[Z/H]/\Delta \log r = -0.23$; Spolaor et al. 2010, see also Kuntschner et al. 2010; Koleva et al. 2011), the change in $[Z/H]$ integrated within $r_e/8$ and out to $r \gg r_e$ is found to be only $\lesssim 0.05$ dex when coupled with a Sérsic profile with $n \gtrsim 1$ and large PSF size compared to the effective radius. Therefore, our measured $[Z/H]$ appears to be more representative of the central value. Note that the measured indices, hence the derived age, $[Z/H]$, and $[\alpha/Fe]$ presented in Jørgensen & Chiboucas (2013) for intermediate- z cluster galaxies have already been corrected to the values within 3.4 arcsec at the distance of the Coma cluster, based on measurements of index gradients of

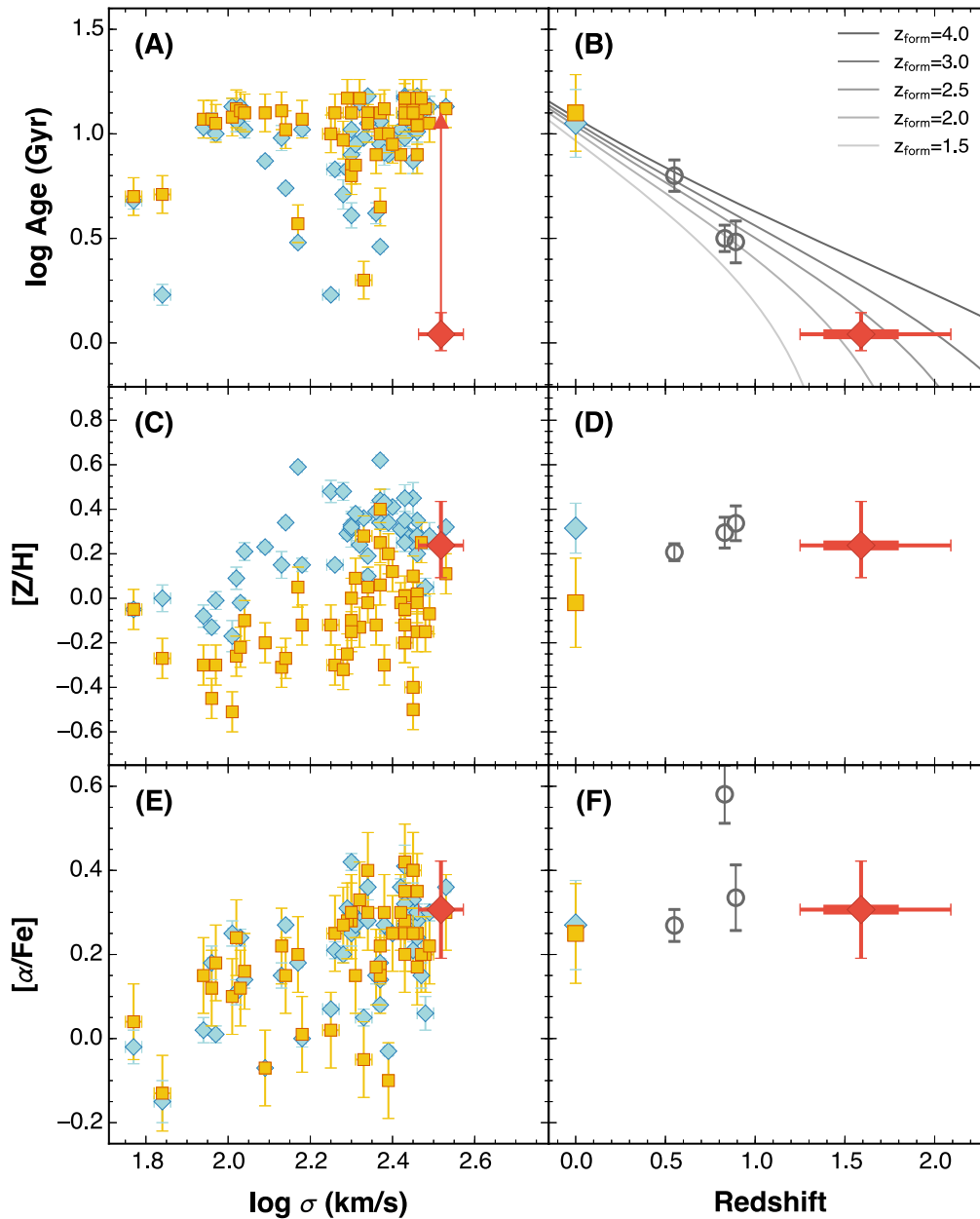


Figure 5. Stellar population parameters as a function of stellar velocity dispersion (A), (C), (E), and redshift (B), (D), (F). Shown are the luminosity-weighted age (A), (B), $[Z/H]$ (C), (D), and the $[\alpha/Fe]$ ratio (E), (F) of stellar populations in quenched galaxies at various redshifts. In each panel, the red symbol represents our measurement at $\langle z \rangle = 1.6$. In the right panels, the thick and thin error bars correspond to the standard deviation and range of redshift of the sample, respectively. Blue and orange symbols show $z = 0$ values within $r_c/8$ and r_c , respectively, of local quenched galaxies (Spolaor et al. 2010). In the right panels, blue and orange points are the corresponding median properties of the local sample with $\sigma > 200 \text{ km s}^{-1}$ with the 1σ scatter of the corresponding distribution. The red arrowhead in panel (A) shows the ending point of a purely passive evolution of the stellar populations of our sample down to $z = 0$. Gray circles in the right panels show the values for massive quenched galaxies with $\log \sigma (\text{km s}^{-1}) > 2.24$ in intermediate redshift clusters (Jørgensen & Chiboucas 2013). Their measurements were aperture corrected in order to match the nuclear measurements at $z = 0$. In panel (B), the gray solid lines show, from thin to thick, the age of simple stellar populations made at a formation redshifts from 1.5 to 4.0, as indicated in the insert.

local galaxies (Jørgensen & Chiboucas 2013, see also Jørgensen et al. 1995; Jørgensen et al. 2005).

The α -to-iron abundance ratio measured for the $\langle z \rangle = 1.6$ quenched galaxies, $[\alpha/Fe] = 0.31^{+0.12}_{-0.12}$, or ~ 2 times the solar value, lies precisely on the $z = 0$ $[\alpha/Fe]$ - σ relation (Figure 5; e.g., Kuntschner et al. 2010; Spolaor et al. 2010; Thomas et al. 2010), indicating little or no evolution at a given velocity dispersion of the $[\alpha/Fe]$ ratio over the past ~ 10 Gyr.

Thus, it appears that the chemical composition is indeed *frozen in* during passive evolution from $\langle z \rangle = 1.6$ to 0. We conclude

that the stellar population content, i.e., their age, metallicity and α -element enhancement of our $\langle z \rangle = 1.6$ galaxies, qualifies them as possible progenitors of similarly massive quenched galaxies at $z = 0$, from purely passive evolution.

5.3. SFHs of Quenched Galaxies at $\langle z \rangle = 1.6$ and Their Precursors

We turn now to the other side in cosmic times, i.e., toward higher redshifts and earlier epochs, trying to identify possible

progenitors of our quenched galaxies at $\langle z \rangle = 1.6$. At higher redshift star-forming galaxies dominate the massive galaxy population (e.g., Ilbert et al. 2013; Muzzin et al. 2013b) and it is among them that precursors should be sought. The average age ~ 1.1 Gyr of our quenched galaxies at $\langle z \rangle = 1.6$ indicates a formation redshift of $z_f \simeq 2.3$ for their stellar populations, as also indicated in Figure 5(B). As already mentioned, having been derived from fits to SSPs, this “age” is essentially a measure of the time elapsed since their star formation was quenched. Indeed, if the SFR was rapidly increasing, as expected for the evolution of main-sequence galaxies at such high redshift (Renzini 2009; Peng et al. 2010b), then the corresponding formation redshift must also be close to the quenching epoch, as most of the stars formed just prior to the quenching. By the same token, these authors argue that an α -element enhancement relative to the solar abundance ratio is the natural outcome of such a (quasi-exponential) rapid increase in SFR.

Following Thomas et al. (2005), we use the measured $[\alpha/\text{Fe}]$ ratio to estimate the star formation timescale of the precursors as $\log(\Delta t/\text{Gyr}) \approx 6 \times \left(\frac{1}{5} - [\alpha/\text{Fe}] \right) = -0.66 \pm 0.72$. Given the large error bars and the approximate nature of this relation, we conservatively adopt a 1σ upper limit of $\Delta t \simeq 1$ Gyr, and translate this timescale into a specific SFR ($s\text{SFR} \equiv \text{SFR}/M$) = $1/\Delta t \simeq 1 \text{ Gyr}^{-1}$. At the median stellar mass of our sample, the corresponding lower limit for the SFR just prior to the quenching is therefore $\text{SFR} \simeq 200 M_\odot \text{ yr}^{-1}$. This matches the measured SFR of main-sequence star-forming galaxies of similar stellar mass at $z \gtrsim 2$ (e.g., Daddi et al. 2007; Pannella et al. 2015; Rodighiero et al. 2014).

As an independent consistency check we have adopted an exponentially rising SFR as appropriate for star-forming main-sequence galaxies at $z \sim 2$ (e.g., Renzini 2009; Maraston et al. 2010; Papovich et al. 2011; Reddy et al. 2012) and have estimated that a SFR culminating at $\sim 300 M_\odot \text{ yr}^{-1}$ just prior to the quenching would be required to build a stellar mass of $2.3 \times 10^{11} M_\odot$ by $z = 2.3$, i.e., at the average quenching epoch and mass for our sample. Again, this is in good agreement with the pre-quenching SFR that we have inferred from the $[\alpha/\text{Fe}]$ ratio.

Detailed studies of massive, $M > 10^{11} M_\odot$ star-forming main-sequence galaxies at $z > 2$ – 2.5 with resolved kpc-scale gas kinematics, SFR and stellar mass densities, and emission line profiles secured in recent years (Förster Schreiber et al. 2009, and N. M. Förster Schreiber et al. 2015, in preparation; Tacchella et al. 2015b) show that their high SFRs are mostly sustained at high galactocentric distances (Genzel et al. 2014b; Tacchella et al. 2015a). By contrast, the central regions of such galaxies are already relatively quenched, and have reached central mass concentrations that are similar to those of $z = 0$ quenched spheroids (Tacchella et al. 2015a). These inner quenched spheroidal components argue for an inside-out quenching process, as expected, for example, in the case of AGN feedback or gravitational quenching (but see Sargent et al. 2015). Moreover, these galaxies show strong nuclear outflows running at up to $\sim 1600 \text{ km s}^{-1}$, which are most likely driven by AGN feedback (Cimatti et al. 2013; Förster Schreiber et al. 2014; Genzel et al. 2014a). These outflows provide tantalizing support for AGN-related processes being responsible for quenching, though evidence for AGN feedback is not necessarily evidence for AGN quenching.

These $z \gtrsim 2$ galaxies qualify as possible precursors to our quenched galaxies at $z \sim 1.6$ for two reasons. First, all $z \sim 2.3$ massive galaxies on the main sequence must soon be quenched, otherwise they would dramatically overgrow (Renzini 2009; Peng et al. 2010b). Second, their properties (described above) indicate that the quenching process may already be under way. These observations seem to support the notion that *mass quenching* of star formation in massive galaxies (Peng et al. 2010b) is predominantly a rapid process, as opposed to an slow quenching process such as halo quenching (Woo et al. 2015, but see Knobel et al. 2015).

5.4. Size Growth and Progenitor Bias

As we showed above, a purely passive evolution of our quenched galaxies to $z \sim 0$, i.e., without any further star formation, will bring their stellar population properties to closely match their counterparts in the local universe. However, quenched galaxies at high redshifts are known to have smaller sizes compared to local galaxies (e.g., Daddi et al. 2005; Trujillo et al. 2006; Cimatti et al. 2008; van Dokkum et al. 2008; Cassata et al. 2011; van der Wel et al. 2014). The average effective radius of 2.7 kpc that we have measured for the 24 $\langle z \rangle = 1.6$ galaxies is, indeed, a factor of ~ 2.5 smaller than that of local quenched galaxies of the same stellar mass (Table 1; Newman et al. 2012). Two main processes have been suggested and extensively discussed as being responsible for the average size growth of the quenched galaxy population: the growth of individual galaxies and the addition of larger-sized quenched galaxies at later epochs (Carollo et al. 2013). A series of minor *dry* mergers with other quenched galaxies is one effective way to increase the sizes of individual galaxies, by adding an extended envelope to a pre-existing compact galaxy (e.g., Hopkins et al. 2009; Naab et al. 2009; Cappellari 2013). Based on the study of abundance ratios of different elements, Greene et al. (2012, 2013) found that stellar populations in the outskirts ($\gtrsim 2r_e$) of nearby massive early-type galaxies ($\sigma_* \gtrsim 150 \text{ km s}^{-1}$) are different from those in the inner regions, as they are composed of similarly old (~ 10 Gyr) but more metal-poor ($[\text{Fe}/\text{H}] \sim -0.5$) and α -element enhanced ($[\alpha/\text{Fe}] \sim 0.3$) stars. They argue that these distinct stellar populations have formed at $z > 1.5$ – 2 in less massive systems and then accreted onto the outskirts of massive quenched galaxies. This scenario is consistent with our results, as the stellar population parameters of both low and high-redshift galaxies considered here were measured essentially within the central part of the galaxies.

One problem with this mechanism for growing galaxies is that it requires minor merging events to be gas-poor, otherwise gas would sink to the bottom of the potential well, leading to further star formation and resulting in an even more compact galaxy (Naab et al. 2009). However, at $z \gtrsim 1.5$ most galaxies appear to be gas-rich and forming stars (e.g., Daddi et al. 2010; Tacconi et al. 2010, 2013; Sargent et al. 2014), and it seems rather difficult for massive quenched galaxies to accrete selectively quenched galaxies and avoid gas accretion and subsequent star formation. Still, one may speculate that *galactic conformity*, the phenomenon that satellites of quenched centrals are more likely to be quenched even out to $z \lesssim 2$ (e.g., Weinmann et al. 2006; Hartley et al. 2015; Knobel et al. 2015), might help make small systems quiescent before they are accreted. Moreover, Williams et al. (2011) and Newman et al. (2012) do not find a sufficient number of

satellites around massive quenched galaxies to account for their size growth between $z = 2$ and 1.

Thus an alternative or additional process to secularly grow the average size of quenched galaxies needs to be considered. At stellar masses $\gtrsim 10^{11} M_{\odot}$, the number density of quenched galaxies increases by about one order of magnitude between $z = 2$ and $z = 0$ (e.g., Cassata et al. 2013; Muzzin et al. 2013b), with most of the increase for massive galaxies having taken place by $z \sim 1$ (e.g., Cimatti et al. 2006). Thus, it has been argued that at least part of the evolution in the average size of quenched galaxies should be due to the continuous addition of quenched galaxies that are already larger than those formed at earlier times (e.g., Carollo et al. 2013; Poggianti et al. 2013). Indeed, the average size of star-forming galaxies also increases with time, running above and nearly parallel to the average size of quenched galaxies (van der Wel et al. 2014). Therefore, newly quenched galaxies are likely to be larger than pre-existing ones and also smaller than the star-forming progenitors due to the fast fading of the quenched disk (Carollo et al. 2014). This effect, a kind of *progenitor bias*, could explain some of the apparent size evolution of quenched galaxy populations, given the mentioned difficulties of the scenario invoking the size growth of individual galaxies, though the two effects are also likely to work together (Belli et al. 2015).

For these reasons, a comparison between galaxy populations at different redshifts and fixed stellar masses could suffer from this progenitor bias. However, Bezanson et al. (2012) showed that the number density of quiescent galaxies with large σ_{inf} ($\gtrsim 250 \text{ km s}^{-1}$) is remarkably constant at $0.3 < z < 1.5$, which indicates that the build-up of quiescent galaxy populations with high velocity dispersions was largely completed by $z \sim 1.5$. Thus, a comparison based on stellar velocity dispersions could greatly reduce the effect of the progenitor bias. Indeed, in Figure 5 essentially all of the nearby early-type galaxies presented in Spolaor et al. (2010) with $\sigma_{*} > 250 \text{ km s}^{-1}$ have stellar population ages $\gtrsim 10 \text{ Gyr}$. The age distribution of morphologically selected SDSS early-type galaxies with $\sigma_{*} \gtrsim 250 \text{ km s}^{-1}$ at $0.05 < z < 0.06$ also peaks at an age of $\approx 10 \text{ Gyr}$ (Thomas et al. 2010), which is in good agreement with the expected age for our $\langle z \rangle = 1.6$ sample assuming pure passive evolution down to $z \sim 0.05$.

6. SUMMARY

Using a rest-frame optical composite spectrum of 24 massive quenched galaxies at $\langle z \rangle = 1.6$ and with $\langle M \rangle = 2.5 \times 10^{11} M_{\odot}$, we have derived luminosity-weighted stellar population parameters from Lick absorption line indices, namely age, $[Z/H]$, and $[\alpha/\text{Fe}]$, and have discussed their past SFH and subsequent evolution toward lower redshifts, identifying the likely progenitors and descendants of similar galaxies. Our main results can be summarized as follows.

1. The average stellar population properties derived are $\log(\text{age}/\text{Gyr}) = 0.04_{-0.08}^{+0.10}$, or $\sim 1.1 \text{ Gyr}$, $[Z/H] = 0.24_{-0.14}^{+0.20}$, and $[\alpha/\text{Fe}] = 0.31_{-0.12}^{+0.12}$. The average stellar velocity dispersion of these galaxies is $\sigma_{*} = 330 \pm 41 \text{ km s}^{-1}$, as measured from the composite spectrum.
2. The $\langle z \rangle = 1.6$ galaxies show $[Z/H]$ and $[\alpha/\text{Fe}]$ in excellent agreement with those of local early-type galaxies at similar velocity dispersions. Pure passive evolution to $z = 0$ brings the age of these $\langle z \rangle = 1.6$ quenched galaxies to coincide with that of their local

counterparts at the same σ_{*} . Therefore, the stellar populations of the galaxies in our sample qualify such galaxies as plausible progenitors of similarly massive quenched galaxies in the local universe.

3. The age of 1.1 Gyr for the bulk of stars in these galaxies points to a formation redshift of $z_f \sim 2.3$, an epoch when massive galaxies on the main sequence are very rapidly growing in mass and therefore must soon be quenched.
4. The $[\alpha/\text{Fe}]$ value indicates a star formation timescale of $\Delta t \lesssim 1 \text{ Gyr}$ which in turn implies a typical SFR of $\sim 200 M_{\odot} \text{ yr}^{-1}$ just prior to the quenching. This SFR is well within a range covered by similarly massive main-sequence galaxies at $z \sim 2.3$.
5. These properties of massive $z \sim 2.3$ main-sequence galaxies qualify them as likely precursors to our quenched galaxy at $\langle z \rangle = 1.6$.

One limitation of the present study is that we had to stack individual spectra to an equivalent integration time of $\sim 200 \text{ hr}$ in order to achieve a high S/N that was adequate for the analysis of the Lick indices. Further studies based on high S/N spectra of individual galaxies are needed to account for a diversity in high-redshift quenched galaxy populations (e.g., Belli et al. 2015). This is becoming possible through deep absorption line spectroscopy with the new generation of near-IR spectrographs such as Keck/MOSFIRE and VLT/KMOS, though very long integration times will still be necessary.

We are grateful to the referee for useful and constructive comments. We thank the staff of the Subaru telescope, especially Ichi Tanaka, for supporting the observations. We also thank Sumire Tatehara, Will Hartley, Claudia Maraston, Daniel Thomas, and Alexandre Vazdekis for fruitful discussions, and Joanna Woo for reading the manuscript thoughtfully. We acknowledge Inger Jørgensen for providing us with measurements in electronic form. This work has been partially supported by the Grant-in-aid for the Scientific Research Fund under grant No. 23224005, and the Program for Leading Graduate Schools PhD Professional: Gateway to Success in Frontier Asia, commissioned by the Ministry of Education, Culture, Sports, Science and Technology (MEXT) of Japan. This research made extensive use of *Astropy*,²¹ a community-developed core Python package for Astronomy (Astropy Collaboration et al. 2013), and *matplotlib*,²² a Python 2D plotting library (Hunter 2007).

Facilities: Subaru (MOIRCS)

REFERENCES

- Astropy Collaboration, Robitaille, T. P., Tollerud, E. J., et al. 2013, *A&A*, **558**, A33
- Bedregal, A. G., Scarlata, C., Henry, A. L., et al. 2013, *ApJ*, **778**, 126
- Beers, T. C., Flynn, K., & Gebhardt, K. 1990, *AJ*, **100**, 32
- Belli, S., Newman, A. B., & Ellis, R. S. 2014a, *ApJ*, **783**, 117
- Belli, S., Newman, A. B., & Ellis, R. S. 2015, *ApJ*, **799**, 206
- Belli, S., Newman, A. B., Ellis, R. S., & Konidaris, N. P. 2014b, *ApJL*, **788**, L29
- Bezanson, R., van Dokkum, P., & Franx, M. 2012, *ApJ*, **760**, 62
- Bezanson, R., van Dokkum, P., van de Sande, J., Franx, M., & Kriek, M. 2013, *ApJL*, **764**, L8
- Bezanson, R., van Dokkum, P. G., Franx, M., et al. 2011, *ApJL*, **737**, L31
- Birboim, Y., & Dekel, A. 2003, *MNRAS*, **345**, 349
- Bouché, N., Dekel, A., Genzel, R., et al. 2010, *ApJ*, **718**, 1001

²¹ <http://www.astropy.org>

²² <http://matplotlib.org>

- Brammer, G. B., van Dokkum, P. G., & Coppi, P. 2008, *ApJ*, **686**, 1503
- Brammer, G. B., van Dokkum, P. G., Franx, M., et al. 2012, *ApJS*, **200**, 13
- Brinchmann, J., Charlot, S., White, S. D. M., et al. 2004, *MNRAS*, **351**, 1151
- Bruzual, G., & Charlot, S. 2003, *MNRAS*, **344**, 1000
- Burstein, D., Faber, S. M., Gaskell, C. M., & Krumm, N. 1984, *ApJ*, **287**, 586
- Calzetti, D., Armus, L., Bohlin, R. C., et al. 2000, *ApJ*, **533**, 682
- Cappellari, M. 2013, *ApJL*, **778**, L2
- Cappellari, M., & Emsellem, E. 2004, *PASP*, **116**, 138
- Cappellari, M., di Serego Alighieri, S., Cimatti, A., et al. 2009, *ApJL*, **704**, L34
- Carollo, C. M., Bschorr, T. J., Renzini, A., et al. 2013, *ApJ*, **773**, 112
- Carollo, C. M., Cibinel, A., Lilly, S. J., et al. 2014, arXiv:1402.1172
- Carollo, C. M., Danziger, I. J., & Buson, L. 1993, *MNRAS*, **265**, 553
- Cassata, P., Giavalisco, M., Guo, Y., et al. 2011, *ApJ*, **743**, 96
- Cassata, P., Giavalisco, M., Williams, C. C., et al. 2013, *ApJ*, **775**, 106
- Choi, J., Conroy, C., Moustakas, J., et al. 2014, *ApJ*, **792**, 95
- Cimatti, A., Brusa, M., Talia, M., et al. 2013, *ApJL*, **779**, L13
- Cimatti, A., Cassata, P., Pozzetti, L., et al. 2008, *A&A*, **482**, 21
- Cimatti, A., Daddi, E., & Renzini, A. 2006, *A&A*, **453**, L29
- Cimatti, A., Daddi, E., Renzini, A., et al. 2004, *Natur*, **430**, 184
- Conroy, C., Graves, G. J., & van Dokkum, P. G. 2014, *ApJ*, **780**, 33
- Croton, D. J., Springel, V., White, S. D. M., et al. 2006, *MNRAS*, **365**, 11
- Daddi, E., Bournaud, F., Walter, F., et al. 2010, *ApJ*, **713**, 686
- Daddi, E., Cimatti, A., Renzini, A., et al. 2004, *ApJ*, **617**, 746
- Daddi, E., Dickinson, M., Morrison, G., et al. 2007, *ApJ*, **670**, 156
- Daddi, E., Renzini, A., Pirzkal, N., et al. 2005, *ApJ*, **626**, 680
- Davé, R., Finlator, K., & Oppenheimer, B. D. 2012, *MNRAS*, **421**, 98
- Dekel, A., Birnboim, Y., Engel, G., et al. 2009, *Natur*, **457**, 451
- Elbaz, D., Daddi, E., Le Borgne, D., et al. 2007, *A&A*, **468**, 33
- Förster Schreiber, N. M., Genzel, R., Bouché, N., et al. 2009, *ApJ*, **706**, 1364
- Förster Schreiber, N. M., Genzel, R., Newman, S. F., et al. 2014, *ApJ*, **787**, 38
- Gallazzi, A., Bell, E. F., Zibetti, S., Brinchmann, J., & Kelson, D. D. 2014, *ApJ*, **788**, 72
- Genzel, R., Förster Schreiber, N. M., Lang, P., et al. 2014b, *ApJ*, **785**, 75
- Genzel, R., Förster Schreiber, N. M., Rosario, D., et al. 2014a, *ApJ*, **796**, 7
- Glazebrook, K., Abraham, R. G., McCarthy, P. J., et al. 2004, *Natur*, **430**, 181
- Gobat, R., Strazzullo, V., Daddi, E., et al. 2012, *ApJL*, **759**, L44
- Gobat, R., Strazzullo, V., Daddi, E., et al. 2013, *ApJ*, **776**, 9
- Greene, J. E., Murphy, J. D., Comerford, J. M., Gebhardt, K., & Adams, J. J. 2012, *ApJ*, **750**, 32
- Greene, J. E., Murphy, J. D., Graves, G. J., et al. 2013, *ApJ*, **776**, 64
- Hartley, W. G., Conselice, C. J., Mortlock, A., Foucaud, S., & Simpson, C. 2015, *MNRAS*, **451**, 1613
- Hopkins, P. F., Hernquist, L., Cox, T. J., et al. 2006, *ApJS*, **163**, 1
- Hopkins, P. F., Hernquist, L., Cox, T. J., Keres, D., & Wuyts, S. 2009, *ApJ*, **691**, 1424
- Hunter, J. D. 2007, *CSE*, **9**, 90
- Ichikawa, T., Suzuki, R., Tokoku, C., et al. 2006, *Proc. SPIE*, **6269**, 16
- Ilbert, O., McCracken, H. J., Le Fèvre, O., et al. 2013, *A&A*, **556**, A55
- Jørgensen, I., Bergmann, M., Davies, R., et al. 2005, *AJ*, **129**, 1249
- Jørgensen, I., & Chiboucas, K. 2013, *AJ*, **145**, 77
- Jørgensen, I., Franx, M., & Kjaergaard, P. 1995, *MNRAS*, **276**, 1341
- Karim, A., Schinnerer, E., Martínez-Sansigre, A., et al. 2011, *ApJ*, **730**, 61
- Kashino, D., Silverman, J. D., Rodighiero, G., et al. 2013, *ApJL*, **777**, L8
- Kelson, D. D. 2014, arXiv:1406.5191
- Kelson, D. D., Illingworth, G. D., Franx, M., & van Dokkum, P. G. 2001, *ApJL*, **552**, L17
- Kelson, D. D., Illingworth, G. D., Franx, M., & van Dokkum, P. G. 2006, *ApJ*, **653**, 159
- Knobel, C., Lilly, S. J., Woo, J., & Kovač, K. 2015, *ApJ*, **800**, 24
- Kobayashi, C., & Arimoto, N. 1999, *ApJ*, **527**, 573
- Koekemoer, A. M., Aussel, H., Calzetti, D., et al. 2007, *ApJS*, **172**, 196
- Koleva, M., Prugniel, P., de Rijcke, S., & Zeilinger, W. W. 2011, *MNRAS*, **417**, 1643
- Kriek, M., van Dokkum, P. G., Franx, M., et al. 2008, *ApJ*, **677**, 219
- Kriek, M., van Dokkum, P. G., Labbé, I., et al. 2009, *ApJ*, **700**, 221
- Krogager, J.-K., Zirm, A. W., Toft, S., Man, A., & Brammer, G. 2014, *ApJ*, **797**, 17
- Kuntschner, H., Emsellem, E., Bacon, R., et al. 2010, *MNRAS*, **408**, 97
- Lilly, S. J., Carollo, C. M., Pipino, A., Renzini, A., & Peng, Y. 2013, *ApJ*, **772**, 119
- Magdis, G. E., Rigopoulou, D., Huang, J.-S., & Fazio, G. G. 2010, *MNRAS*, **401**, 1521
- Maíz Apellániz, J. 2006, *AJ*, **131**, 1184
- Maraston, C., Pforr, J., Renzini, A., et al. 2010, *MNRAS*, **407**, 830
- Martig, M., Bournaud, F., Teysseier, R., & Dekel, A. 2009, *ApJ*, **707**, 250
- Massey, R., Stoughton, C., Leauthaud, A., et al. 2010, *MNRAS*, **401**, 371
- Matteucci, F., & Greggio, L. 1986, *A&A*, **154**, 279
- McCracken, H. J., Capak, P., Salvato, M., et al. 2010, *ApJ*, **708**, 202
- Moresco, M., Pozzetti, L., Cimatti, A., et al. 2013, *A&A*, **558**, A61
- Muzzin, A., Marchesini, D., Stefanon, M., et al. 2013a, *ApJS*, **206**, 8
- Muzzin, A., Marchesini, D., Stefanon, M., et al. 2013b, *ApJ*, **777**, 18
- Naab, T., Johansson, P. H., & Ostriker, J. P. 2009, *ApJL*, **699**, L178
- Newman, A. B., Ellis, R. S., Bundy, K., & Treu, T. 2012, *ApJ*, **746**, 162
- Noeske, K. G., Weiner, B. J., Faber, S. M., et al. 2007, *ApJL*, **660**, L43
- Oke, J. B., & Gunn, J. E. 1983, *ApJ*, **266**, 713
- Onodera, M., Daddi, E., Gobat, R., et al. 2010, *ApJL*, **715**, L6
- Onodera, M., Renzini, A., Carollo, M., et al. 2012, *ApJ*, **755**, 26
- Pannella, M., Carilli, C. L., Daddi, E., et al. 2009, *ApJL*, **698**, L116
- Pannella, M., Elbaz, D., Daddi, E., et al. 2015, *ApJ*, **807**, 141
- Papovich, C., Finkelstein, S. L., Ferguson, H. C., Lotz, J. M., & Giavalisco, M. 2011, *MNRAS*, **412**, 1123
- Peng, C. Y., Ho, L. C., Impey, C. D., & Rix, H.-W. 2002, *AJ*, **124**, 266
- Peng, C. Y., Ho, L. C., Impey, C. D., & Rix, H.-W. 2010a, *AJ*, **139**, 2097
- Peng, Y.-j., Lilly, S. J., Kovač, K., et al. 2010b, *ApJ*, **721**, 193
- Poggianti, B. M., Moretti, A., Calvi, R., et al. 2013, *ApJ*, **777**, 125
- Poole, V., Worthey, G., Lee, H.-c., & Serven, J. 2010, *AJ*, **139**, 809
- Reddy, N. A., Pettini, M., Steidel, C. C., et al. 2012, *ApJ*, **754**, 25
- Renzini, A. 2009, *MNRAS*, **398**, L58
- Rodighiero, G., Daddi, E., Baronchelli, I., et al. 2011, *ApJL*, **739**, L40
- Rodighiero, G., Renzini, A., Daddi, E., et al. 2014, *MNRAS*, **443**, 19
- Salmi, F., Daddi, E., Elbaz, D., et al. 2012, *ApJL*, **754**, L14
- Salpeter, E. E. 1955, *ApJ*, **121**, 161
- Sánchez-Blázquez, P., Gorgas, J., Cardiel, N., & González, J. J. 2006a, *A&A*, **457**, 809
- Sánchez-Blázquez, P., Peletier, R. F., Jiménez-Vicente, J., et al. 2006b, *MNRAS*, **371**, 703
- Sargent, M. T., Daddi, E., Béthermin, M., et al. 2014, *ApJ*, **793**, 19
- Sargent, M. T., Daddi, E., & Bournaud, F. 2015, *ApJL*, **806**, L20
- Schiavon, R. P. 2007, *ApJS*, **171**, 146
- Scoville, N., Aussel, H., Brusa, M., et al. 2007, *ApJS*, **172**, 1
- Shetty, S., & Cappellari, M. 2014, *ApJL*, **786**, L10
- Speagle, J. S., Steinhardt, C. L., Capak, P. L., & Silverman, J. D. 2014, *ApJS*, **214**, 15
- Spolaor, M., Kobayashi, C., Forbes, D. A., Couch, W. J., & Hau, G. K. T. 2010, *MNRAS*, **408**, 272
- Suzuki, R., Tokoku, C., Ichikawa, T., et al. 2008, *PASJ*, **60**, 1347
- Tacchella, S., Carollo, C. M., Renzini, A., et al. 2015a, *Sci*, **348**, 314
- Tacchella, S., Lang, P., Carollo, C. M., et al. 2015b, *ApJ*, **802**, 101
- Tacconi, L. J., Genzel, R., Neri, R., et al. 2010, *Natur*, **463**, 781
- Tacconi, L. J., Neri, R., Genzel, R., et al. 2013, *ApJ*, **768**, 74
- Thomas, D., Greggio, L., & Bender, R. 1999, *MNRAS*, **302**, 537
- Thomas, D., Johansson, J., & Maraston, C. 2011a, *MNRAS*, **412**, 2199
- Thomas, D., Maraston, C., & Bender, R. 2003, *MNRAS*, **339**, 897
- Thomas, D., Maraston, C., Bender, R., & Mendes de Oliveira, C. 2005, *ApJ*, **621**, 673
- Thomas, D., Maraston, C., & Johansson, J. 2011b, *MNRAS*, **412**, 2183
- Thomas, D., Maraston, C., Schawinski, K., Sarzi, M., & Silk, J. 2010, *MNRAS*, **404**, 1775
- Toft, S., Gallazzi, A., Zirm, A., et al. 2012, *ApJ*, **754**, 3
- Trager, S. C., Faber, S. M., & Dressler, A. 2008, *MNRAS*, **386**, 715
- Trager, S. C., Faber, S. M., Worthey, G., & González, J. J. 2000, *AJ*, **119**, 1645
- Trager, S. C., Worthey, G., Faber, S. M., Burstein, D., & Gonzalez, J. J. 1998, *ApJS*, **116**, 1
- Trujillo, I., Förster Schreiber, N. M., Rudnick, G., et al. 2006, *ApJ*, **650**, 18
- van de Sande, J., Kriek, M., Franx, M., Bezanson, R., & van Dokkum, P. G. 2014, *ApJL*, **793**, L31
- van de Sande, J., Kriek, M., Franx, M., et al. 2011, *ApJL*, **736**, L9
- van de Sande, J., Kriek, M., Franx, M., et al. 2013, *ApJ*, **771**, 85
- van der Wel, A., Franx, M., van Dokkum, P. G., et al. 2014, *ApJ*, **788**, 28
- van Dokkum, P. G., Franx, M., Kriek, M., et al. 2008, *ApJL*, **677**, L5
- Vazdekis, A., Sánchez-Blázquez, P., Falcón-Barroso, J., et al. 2010, *MNRAS*, **404**, 1639
- Weinmann, S. M., van den Bosch, F. C., Yang, X., & Mo, H. J. 2006, *MNRAS*, **366**, 2
- Whitaker, K. E., Kriek, M., van Dokkum, P. G., et al. 2012a, *ApJ*, **745**, 179
- Whitaker, K. E., van Dokkum, P. G., Brammer, G., & Franx, M. 2012b, *ApJL*, **754**, L29
- Whitaker, K. E., Franx, M., Leja, J., et al. 2014, *ApJ*, **795**, 104
- Whitaker, K. E., van Dokkum, P. G., Brammer, G., et al. 2013, *ApJL*, **770**, L39

- Williams, R. J., Quadri, R. F., & Franx, M. 2011, [ApJL](#), **738**, L25
- Williams, R. J., Quadri, R. F., Franx, M., van Dokkum, P., & Labbé, I. 2009, [ApJ](#), **691**, 1879
- Woo, J., Dekel, A., Faber, S. M., & Koo, D. C. 2015, [MNRAS](#), **448**, 237
- Worthey, G., Faber, S. M., Gonzalez, J. J., & Burstein, D. 1994, [ApJS](#), **94**, 687
- Worthey, G., & Ottaviani, D. L. 1997, [ApJS](#), **111**, 377
- Yamada, Y., Arimoto, N., Vazdekis, A., & Peletier, R. F. 2006, [ApJ](#), **637**, 200
- Yoshikawa, T., Akiyama, M., Kajisawa, M., et al. 2010, [ApJ](#), **718**, 112